






Disordered hyperuniform quasi-one-dimensional materialsDuyu Chen ^{1,*},† Yu Liu ^{2,*}, Yu Zheng,³ Houlong Zhuang ⁴, Mohan Chen ², and Yang Jiao ^{5,3}¹Materials Research Laboratory, University of California, Santa Barbara, California 93106, USA²HEDPS, Center for Applied Physics and Technology, School of Physics and College of Engineering, Peking University, Beijing 100871, People's Republic of China³Department of Physics, Arizona State University, Tempe, Arizona 85287, USA⁴Mechanical and Aerospace Engineering, Arizona State University, Tempe, Arizona 85287, USA⁵Materials Science and Engineering, Arizona State University, Tempe, Arizona 85287, USA

(Received 30 August 2022; revised 25 November 2022; accepted 13 December 2022; published 23 December 2022)

Carbon nanotubes are quasi-one-dimensional systems that possess large electronic conductance (for the metallic variants), high mechanical strength, selective emission and detection of light, and can be made chemically functionalized. In this work, we generalize the notion of disorder hyperuniformity, a recently discovered exotic state of matter with hidden long-range order, to quasi-one-dimensional materials. As a proof of concept, we then apply the generalized framework to quantify the density fluctuations in amorphous carbon nanotubes containing randomly distributed Stone-Wales defects. We demonstrate that all of these amorphous nanotubes are hyperuniform; i.e., the infinite-wavelength (normalized) density fluctuations of these systems are completely suppressed, regardless of the diameter, rolling axis, number of rolling sheets, and defect fraction of the nanotubes. We find that these amorphous nanotubes are energetically more stable than nanotubes with periodically distributed Stone-Wales defects. Moreover, certain semiconducting defect-free carbon nanotubes become metallic as sufficiently large amounts of defects are randomly introduced. This structural study of amorphous nanotubes strengthens our fundamental understanding of these systems, and suggests possible exotic physical properties, as endowed by their disordered hyperuniformity. Our findings also shed light on the effect of dimensionality reduction on the hyperuniformity property of materials.

DOI: [10.1103/PhysRevB.106.235427](https://doi.org/10.1103/PhysRevB.106.235427)**I. INTRODUCTION**

Carbon nanotubes, a class of quasi-one-dimensional (quasi-1D) materials that can be conceptually constructed by rolling a graphene sheet, have been investigated extensively since their discovery [1,2]. Benefiting from their desirable physical, chemical, and mechanical properties, crystalline carbon nanotubes are popular candidates for a variety of applications, such as field-effect transistors [3], rectifiers [4], and sensors [5]. However, the industrial production of carbon nanotubes (e.g., by catalytic chemical vapor deposition) is still not sufficiently well controlled and various defects can form during nanotube growth [6]. Thus, it is crucial to understand how the defects affect the physical properties and performance of carbon nanotubes. For example, Robinson *et al.* demonstrated controlled introduction of oxidation defects can enhance sensitivity of a single-walled carbon nanotube (SWNT) network sensor to a variety of chemical vapors [7]. Recently, Gifford *et al.* investigated the effect of the sp^3 -hybridized defects on the energies of the optical emissive features and the influence of synthetic modifications on the resulting defect geometry toward attaining desired narrow photoluminescence capacity [8].

A variety of SWNTs can be formed by rolling up an infinitely long strip of a single graphene sheet along different directions. Conventionally, the type of SWNT can be specified by a rolling vector (n, m) (with $n > 0$, $m \geq 0$, and $n \geq m$) in the basis of two linearly independent vectors that connect a carbon atom in the graphene sheet to either two of its nearest atoms with the same bond directions [9]. The two most common types of SWNTs are (i) zigzag nanotubes with $n > 0$ and $m = 0$, and (ii) armchair nanotubes with $n = m$. Multiwalled nanotubes (MWNTs) consisting of purely zigzag nanotubes, purely armchair nanotubes, or a mixture of both are also of great interest. A type of commonly seen defect in covalently bonded network materials is the Stone-Wales (SW) topological defect [10]. A SW topological defect rotates a bond in the network by 90 degrees, transforming 4 adjacent hexagons into a pair of pentagons and a pair of heptagons in the absence of adjacent SW defects. Experimentally, the SW defects can be introduced into carbon nanotubes via high-energy radiations, during the synthesis of materials, or by applying strains [6]. In Fig. 1 we schematically show the generation of a defected (3,0) zigzag nanotube and a defected (3,3) armchair nanotube with SW defects. Previous computational studies have also investigated the effect of the orientation and concentration of SW defects on the electronic properties of various single-walled carbon nanotubes at low defect concentrations [11–13]. However, a comprehensive study of large-scale structures of carbon nanotubes with SW

*The first two authors contributed equally to this work.

†Corresponding author: duyu@alumni.princeton.edu

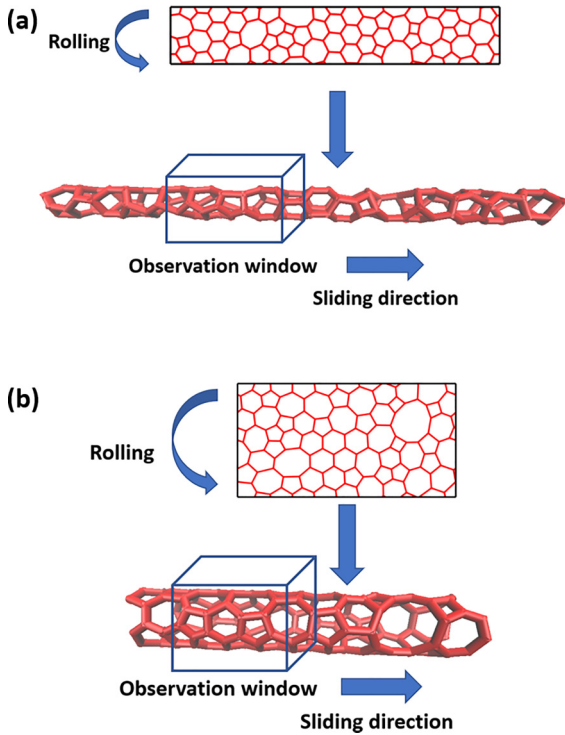


FIG. 1. Illustration of a defected (3,0) zigzag (a) nanotube and a defected (3,3) armchair (b) nanotube formed by rolling graphene sheets with randomly distributed Stone-Wales defects along different rolling directions in two dimensions.

defects across a large range of defect concentrations is still lacking.

Very recently, it has been found that the SW defects in a variety of two-dimensional (2D) material systems, including amorphous 2D silica [14], amorphous graphene [15], defected transition metal dichalcogenides [16], and defected pentagonal 2D materials [17], can lead to special amorphous states [14,15,17,18], in which the density fluctuations in the materials are largely suppressed, a property termed “hyperuniformity.” Interestingly, it was found that the disordered hyperuniform (DHU) states of these materials usually possess a significantly lower energy than other disorder models, suggesting the stability of DHU states for these systems over other disorder models. Moreover, DHU states can lead to unique electronic and thermal transport properties, which are due to mechanisms distinct from those that have been identified for their crystalline counterparts. A key discovery is that the SW defects in these systems play a significant role in establishing hyperuniformity of these 2D material systems [15].

Disordered hyperuniformity is a recently discovered exotic state of matter [19,20], which lies between a perfect crystal and liquid. DHU systems are similar to liquids or glasses in that they are statistically isotropic and possess no Bragg peaks, and yet they completely suppress large-scale normalized density fluctuations such as crystals. In this sense, DHU materials possess a hidden long-range order [19–21] similar to that in crystals. DHU is also manifested as the vanishing of static structure factor $S(k)$ in the infinite-wavelength (or

zero-wave-number) limit, i.e.,

$$\lim_{k \rightarrow 0} S(k) = 0, \quad (1)$$

where k is the wave number [19,20]. Here $S(k)$ is defined as $S(k) \equiv 1 + \rho \tilde{h}(k)$, where $\tilde{h}(k)$ is the Fourier transform of the total correlation function $h(r) = g_2(r) - 1$, $g_2(r)$ is the pair correlation function, and ρ is the number density of the system. Note that this definition implies that the forward scattering contribution to the diffraction pattern is omitted. For computational purposes, $S(k)$ is the angular-averaged version of $S(\mathbf{k})$, which can be obtained directly from the particle positions \mathbf{r}_j , i.e.,

$$S(\mathbf{k}) = \frac{1}{N} \left| \sum_{j=1}^N \exp(i\mathbf{k} \cdot \mathbf{r}_j) \right|^2 \quad (\mathbf{k} \neq \mathbf{0}), \quad (2)$$

where N is the total number of points in the system [21], and \mathbf{k} is the wave vector. Equivalently, the local number variance $\sigma_N^2(R) \equiv \langle N^2(R) \rangle - \langle N(R) \rangle^2$ associated with a spherical observation window of radius R grows more slowly than the window volume for DHU systems in the large- R limit [19,20], i.e.,

$$\lim_{R \rightarrow \infty} \frac{\sigma_N^2(R)}{R^d} = 0, \quad (3)$$

where $N(R)$ is the number of particles in a spherical window with radius R randomly placed into the system, R^d is proportional to the observation window volume, and d the dimensionality of the system. The small- k scaling behavior of $S(k) \sim k^\alpha$ dictates the large- R asymptotic behavior of $\sigma_N^2(R)$, based on which all DHU systems can be categorized into three classes: $\sigma_N^2(R) \sim R^{d-1}$ for $\alpha > 1$ (class I); $\sigma_N^2(R) \sim R^{d-1} \ln(R)$ for $\alpha = 1$ (class II); and $\sigma_N^2(R) \sim R^{d-\alpha}$ for $0 < \alpha < 1$ (class III) [20]. We note that conventional disordered systems, such as the Poisson point patterns that are generated by randomly placing point particles into a simulation box and that mimic the ideal gas systems, are known to be not hyperuniform [19].

Disordered hyperuniformity has been observed in a wide spectrum of physical and material systems [20], in both equilibrium and nonequilibrium, and both classical and quantum mechanical varieties. Examples include the density fluctuations in the early universe [22], maximally random jammed packing of hard particles [23–25], exotic classical ground states of many-body systems [26,27], jammed colloidal systems [28,29], driven systems [30–32], certain quantum ground states [33,34], avian photoreceptor patterns [24], organization of immune systems [35], amorphous silicon [36,37], a wide class of disordered cellular materials [38], dynamic random organizing systems [39–43], electron density distributions [44,45], and vortex distribution in superconductors [46,47], to name but a few.

Since nanotubes can be constructed by rolling the corresponding sheets of 2D materials, it is natural to ask the question: Are these quasi-1D materials containing Stone-Wales topological defects also hyperuniform? In this paper, we address this question by generalizing the notion of hyperuniformity to quasi-1D materials, which can be considered as 1D projections of higher-dimensional structures in this con-

text, and may involve the nontrivial situations where multiple points in the higher-dimensional structures are mapped to the same point in the projection. In particular, we systematically generate a diverse spectrum of amorphous carbon nanotubes by continuously introducing SW topological defects into the crystalline systems, and we quantify the generalized density fluctuations in these systems. We demonstrate that all amorphous nanotubes are hyperuniform; i.e., the infinite-wavelength normalized density fluctuations of these systems are completely suppressed, and the systems possess hidden long-range order, regardless of the diameter, rolling axis, number of rolling sheets, and defect fraction of the nanotubes. This structural study of amorphous nanotubes strengthens our fundamental understanding of these systems, and suggests possible exotic physical properties, as endowed by their disordered hyperuniformity.

The rest of the paper is organized as follows: In Sec. II we discuss the generalization of the hyperuniformity concept to quasi-1D materials. In Sec. III we discuss the procedures to generate various types of carbon nanotubes with randomly distributed SW defects. In Secs. IV and V, we respectively investigate the density fluctuations of single-walled and multiwalled nanotubes, which we use as examples to demonstrate the use of the theoretical framework for analyzing hyperuniformity properties in quasi-1D materials. In Sec. VI, we report the physical properties of the hyperuniform carbon nanotubes, including their stability and density of states. In Sec. VII, we provide concluding remarks and discuss the implications of our work in other quasi-1D material systems.

II. HYPERUNIFORMITY OF QUASI-1D MATERIALS

In this section we introduce the generalization of the hyperuniformity concept to quasi-1D materials. These systems typically have small width in all the directions other than the axial/propagation direction. For example, carbon nanotubes have small finite width in the rolling direction. Since hyperuniformity is a large-scale structural feature, only the density fluctuations along the propagation direction should be relevant in the context of hyperuniformity, and effectively we are looking at 1D projections of the graphene sheets along the axial/propagation direction in the case of carbon nanotubes.

An important issue that we need to address when looking at density fluctuations of low-dimensional projections of higher-dimensional structures is that multiple points in the higher-dimensional structures can be mapped to the same point in the projections. Here we generalize the definition of particle density $\rho(\mathbf{x})$ to be

$$\rho(\mathbf{x}) = \sum_{j=1}^M g_j \delta(\mathbf{x} - \mathbf{x}_j), \quad (4)$$

where M is the number of distinguishable points in the projections, and the *multiplicity* g_j is defined as the number of points in the higher-dimensional structures that are mapped to the given point \mathbf{x}_j in the projections. Accordingly, the structure factor $S(\mathbf{k})$ is generalized to be

$$S(\mathbf{k}) = \frac{1}{G} \left| \sum_{j=1}^M g_j \exp(i\mathbf{k} \cdot \mathbf{x}_j) \right|^2 \quad (\mathbf{k} \neq \mathbf{0}), \quad (5)$$

where $G = \sum_{j=1}^M g_j$. We also generate the concept of $N(R) \equiv \langle N(R; \mathbf{x}_0) \rangle$ associated with $\sigma_N^2(R)$ to be

$$N(R; \mathbf{x}_0) = \sum_{j=1}^M g_j m(\mathbf{x}_j - \mathbf{x}_0; R), \quad (6)$$

where $\langle \dots \rangle$ denotes ensemble average, and $m(\mathbf{x} - \mathbf{x}_0; R)$ is the indicator function of the observation window centered at \mathbf{x}_0 with radius R and is defined as

$$m(\mathbf{x}; \mathbf{R}) = \begin{cases} 1, & |\mathbf{x}| \leq R, \\ 0, & \text{otherwise.} \end{cases} \quad (7)$$

We note that using a 1D observation window to look at $\sigma_N^2(R)$ of the projection is equivalent to using an observation window in the higher dimension that encompasses the quasi-1D materials in the radial directions, but slides in the axial/propagation direction, which is illustrated in Fig. 1. Moreover, since a single point at the location \mathbf{x}_j with multiplicity g_j can also be viewed as g_j different points at the same location \mathbf{x}_j and the latter case is a standard 1D point pattern where the definitions of hyperuniformity from Eq. (1) and Eq. (3) have been shown to be equivalent [19], the equivalence of Eq. (1) and Eq. (3) for the definition of hyperuniformity in the case of multiplicity immediately follows. Nonetheless, in many contexts, e.g., when directly extracting atom locations from projected experimental images and analyzing the pair correlations of atom locations, multiple points at the same projected location could be identified as one, and it would be straightforward to use our generalizations of $S(k)$ and $\sigma_N^2(R)$ as specified in Eqs. (5) and (6) to take into account the particle ‘‘intensity’’ information. With these generalizations of $S(k)$ and $\sigma_N^2(R)$, we can then use the definitions of hyperuniformity specified in Eqs. (1) and (3) for a low-dimensional projection, and use the dimension of the projection for d in Eq. (3).

III. GENERATION OF AMORPHOUS CARBON NANOTUBES CONTAINING STONE-WALES DEFECTS

To generate a defected $(n, 0)$ zigzag nanotube at a given defect concentration p , we first introduce a prescribed number of randomly distributed SW defects $N_d = N_b p = \frac{3}{2} N p$ into a graphene sheet with finite width L_y in the vertical direction in Fig. 1(a), where $N_b = \frac{3}{2} N$ and N are the number of bonds and atoms in the sheet, respectively, and $L_y = \sqrt{3}n$ is the length of the $(n, 0)$ vector. We then relax the structure according to the procedure described in Ref. [15], and subsequently roll up the sheet along the vertical direction shown in Fig. 1(a). Specifically, for a given atom at location (x, y) in a graphene sheet, its coordinate (x', y', z') in the resulting zigzag nanotube is given by

$$\begin{aligned} x' &= \frac{L_y}{2\pi} \cos\left(\frac{2\pi y}{L_y}\right), \\ y' &= \frac{L_y}{2\pi} \sin\left(\frac{2\pi y}{L_y}\right), \\ z' &= x, \end{aligned} \quad (8)$$

where x and y axis are the horizontal and vertical directions in Fig. 1(a). On the other hand, to generate a defected

armchair nanotube at a given defect concentration p , we first follow a similar procedure described in Ref. [15], but use a graphene sheet with finite width L_x in the horizontal direction in Fig. 1(a), where $L_x = 3n$ is the length of the (n, n) vector. We note that the directions in Fig. 1(b) are rotated by 90 degrees from those in Fig. 1(a) for clear visualization, so the horizontal direction in Fig. 1(a) is the vertical direction in Fig. 1(b). We then roll up the sheet along the horizontal direction shown in Fig. 1(a), or the vertical direction in Fig. 1(b). Specifically, for a given atom at location (x, y) in a graphene sheet, its coordinate (x', y', z') in the resulting armchair nanotube is given by

$$\begin{aligned} x' &= \frac{L_x}{2\pi} \cos\left(\frac{2\pi x}{L_x}\right), \\ y' &= \frac{L_x}{2\pi} \sin\left(\frac{2\pi x}{L_x}\right), \\ z' &= y, \end{aligned} \quad (9)$$

where the x and y axes are the horizontal and vertical directions in Fig. 1(a).

To obtain MWNTs with SW defects consisting of concentric single-walled nanotubes, we simply generate the constituting single-walled nanotubes separately according to the procedures above, and combine the atoms together. This is possible because the aforementioned procedure produces nanotubes that all wrap around the z' axis in three dimensions. For instance, the coordinate (x'_i, y'_i, z'_i) of atom i in the double-walled MWNT consisting of a $(n_1, 0)$ nanotube and a $(n_2, 0)$ nanotube is given by

$$x'_i = \begin{cases} \frac{L_{y,1}}{2\pi} \cos\left(\frac{2\pi y_i}{L_{y,1}}\right), & 1 \leq i \leq N_1, \\ \frac{L_{y,2}}{2\pi} \cos\left(\frac{2\pi y_i}{L_{y,2}}\right), & N_1 + 1 \leq i \leq N_2, \end{cases} \quad (10)$$

$$y'_i = \begin{cases} \frac{L_{y,1}}{2\pi} \sin\left(\frac{2\pi y_i}{L_{y,1}}\right), & 1 \leq i \leq N_1, \\ \frac{L_{y,2}}{2\pi} \sin\left(\frac{2\pi y_i}{L_{y,2}}\right), & N_1 + 1 \leq i \leq N_2, \end{cases} \quad (11)$$

$$z'_i = x_i, \quad (12)$$

where (x_i, y_i) is the coordinate of atom i in the original graphene sheets, N_1 and N_2 are the numbers of atoms in the $(n_1, 0)$ and $(n_2, 0)$ nanotubes, respectively, and $L_{y,1} = \sqrt{3}n_1$ and $L_{y,2} = \sqrt{3}n_2$. On the other hand, the coordinate (x'_i, y'_i, z'_i) of atom i in the double-walled MWNT consisting of an (n_1, n_1) nanotube and an (n_2, n_2) nanotube is given by

$$x'_i = \begin{cases} \frac{L_{x,1}}{2\pi} \cos\left(\frac{2\pi x_i}{L_{x,1}}\right), & 1 \leq i \leq N_1, \\ \frac{L_{x,2}}{2\pi} \cos\left(\frac{2\pi x_i}{L_{x,2}}\right), & N_1 + 1 \leq i \leq N_2, \end{cases} \quad (13)$$

$$y'_i = \begin{cases} \frac{L_{x,1}}{2\pi} \sin\left(\frac{2\pi x_i}{L_{x,1}}\right), & 1 \leq i \leq N_1, \\ \frac{L_{x,2}}{2\pi} \sin\left(\frac{2\pi x_i}{L_{x,2}}\right), & N_1 + 1 \leq i \leq N_2, \end{cases} \quad (14)$$

$$z'_i = y_i, \quad (15)$$

where (x_i, y_i) is the coordinate of atom i in the original graphene sheets, N_1 and N_2 are the numbers of atoms in the (n_1, n_1) and (n_2, n_2) nanotubes, respectively, and $L_{x,1} = 3n_1$ and $L_{x,2} = 3n_2$. For a double-walled MWNT consisting of

an $(n_1, 0)$ nanotube and an (n_2, n_2) nanotube, the coordinate (x'_i, y'_i, z'_i) of atom i is given by

$$x'_i = \begin{cases} \frac{L_{y,1}}{2\pi} \cos\left(\frac{2\pi y_i}{L_{y,1}}\right), & 1 \leq i \leq N_1, \\ \frac{L_{x,2}}{2\pi} \cos\left(\frac{2\pi x_i}{L_{x,2}}\right), & N_1 + 1 \leq i \leq N_2, \end{cases} \quad (16)$$

$$y'_i = \begin{cases} \frac{L_{y,1}}{2\pi} \sin\left(\frac{2\pi y_i}{L_{y,1}}\right), & 1 \leq i \leq N_1, \\ \frac{L_{x,2}}{2\pi} \sin\left(\frac{2\pi x_i}{L_{x,2}}\right), & N_1 + 1 \leq i \leq N_2, \end{cases} \quad (17)$$

$$z'_i = \begin{cases} x_i, & 1 \leq i \leq N_1, \\ y_i, & N_1 + 1 \leq i \leq N_2, \end{cases} \quad (18)$$

where (x_i, y_i) is the coordinate of atom i in the original graphene sheets, N_1 and N_2 are the numbers of atoms in the $(n_1, 0)$ and (n_2, n_2) nanotubes, respectively, and $L_{y,1} = \sqrt{3}n_1$ and $L_{x,2} = 3n_2$.

IV. DENSITY FLUCTUATIONS OF SINGLE-WALLED NANOTUBES

To investigate density fluctuations of zigzag and armchair single-walled nanotubes, we employ the procedures described in Sec. III to generate 10 configurations of (3,0), (5,0), (3,3), and (5,5) nanotubes at each of the given defect concentrations $p = 0.02, 0.04, 0.06, 0.08, 0.10, 0.12, \text{ and } 0.14$. We then compute their local number variance $\sigma_N^2(R)$ and structure factor $S(k)$. This setting also allows us to study the effect of nanotube radius on the structural features of nanotubes.

As a reference, it can be easily seen that defect-free $(n, 0)$ zigzag nanotubes are mapped into two-scale 1D point patterns with $\zeta = \frac{1}{3}$ [19] when projecting onto the cylinder axis of the nanotubes, with n carbon atoms superimposed onto each other at each point in the 1D projected point pattern. Here ζ is the ratio of the distance between the nearest neighbors and the length of the smallest repeating unit in the two-scale 1D patterns [19]. The number variance of the $(n, 0)$ zigzag nanotubes $\sigma_N^2(R)$ can then be determined analytically as

$$\sigma_N^2(R) = n^2 \sigma_{N,D}^2(R), \quad (19)$$

where $\sigma_{N,D}^2(R)$ is the number variance of the projected two-scale 1D point patterns with $\zeta = \frac{1}{3}$ [19]. As a result, $\sigma_N^2(R)$ of defect-free zigzag nanotubes fluctuates around certain constants, whose value depends on n , and these nanotubes are class-I hyperuniform.

As SW defects are introduced into the nanotubes, the structures gradually transition into amorphous ones, which are reflected in their local number variance $\sigma_N^2(R)$. For example, we show the computed $\sigma_N^2(R)$ for (3,0) zigzag nanotubes at different defect fractions p in Fig. 2(a). At low p , $\sigma_N^2(R)$ exhibits ‘‘periodicity’’ in the window radius R , suggesting the reminiscence of the crystalline order in the systems; at large p , $\sigma_N^2(R)$ varies smoothly with damped oscillations as R increases, indicating the emergence of truly amorphous states. Also, by comparing the results of (3,0) zigzag nanotubes in Fig. 2(a) and the results of (5,0) zigzag nanotubes in Fig. 2(b), one can see that at given p , increasing the radius (or decreasing the curvature) of the armchair nanotube increases density fluctuations. Interestingly, the variance $\sigma_N^2(R)$ of these zigzag nanotubes fluctuates around certain constants as R increases at all investigated p , indicating that these structures are class-I

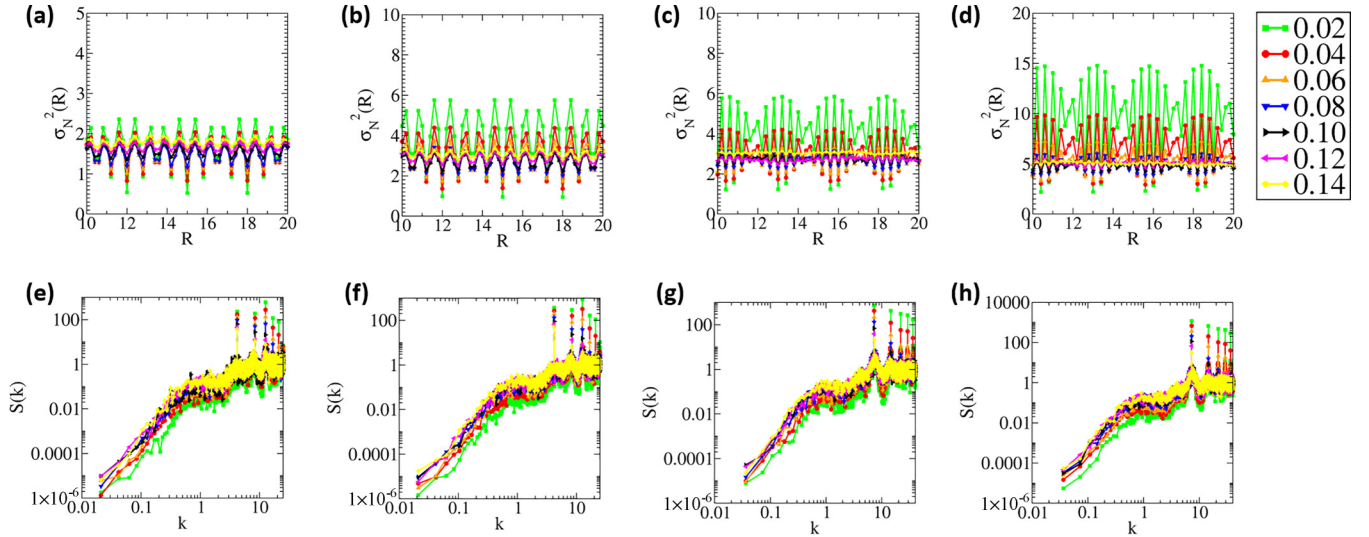


FIG. 2. Local number variances $\sigma_N^2(R)$ (top) and structure factor $S(k)$ (bottom, log-log scale) of defected single-walled zigzag and armchair nanotubes at different defect concentrations p . Column 1: (3,0) zigzag. Column 2: (5,0) zigzag. Column 3: (3,3) armchair. (d) Column 4: (5,5) armchair. The results are all averaged over 10 configurations.

hyperuniform. This is related to the fact that SW transformation and subsequent structural relaxations only result in local rearrangements of atoms, and do not affect the scaling of large-scale density fluctuations in these nanotubes.

Similarly, defect-free (n, n) armchair nanotubes are mapped into single-scale 1D point patterns [19] when projecting onto the cylinder axis of the nanotubes, with $2n$ carbon atoms superimposed onto each other at each point in the 1D point pattern. The number variance of the (n, n) armchair nanotubes $\sigma_N^2(R)$ can then be determined analytically as

$$\sigma_N^2(R) = 4n^2\sigma_{N,S}^2(R), \quad (20)$$

where $\sigma_{N,S}^2(R)$ is the number variance of the projected single-scale 1D pattern. As a result, $\sigma_N^2(R)$ of defect-free armchair nanotubes fluctuates around certain constants, whose value depends on n , and these nanotubes are class-I hyperuniform.

As SW defects are introduced into the nanotubes, the behaviors of these armchair nanotubes are similar to those of the zigzag nanotubes. For example, we show the computed $\sigma_N^2(R)$ for (3,3) armchair nanotubes at different defect fractions p in Fig. 2(c). Importantly, at all investigated p , the variance $\sigma_N^2(R)$ of these armchair nanotubes fluctuates around certain constants, indicating that these structures are hyperuniform. Also, by comparing the results of (3,3) armchair nanotubes in Fig. 2(c) and the results of (5,5) armchair nanotubes in Fig. 2(d), one can see that at given p , increasing the radius (or decreasing the curvature) of the armchair nanotube increases density fluctuations.

The results of ensemble-averaged $S(k)$ of the aforementioned zigzag and armchair nanotubes are shown in Figs. 2(e)–2(h), which all decreases to zero as k goes to zero, regardless of defect concentration p . These results further confirm the hyperuniformity of these nanotubes, and are consistent with the results of $\sigma_N^2(R)$. Moreover, as p increases, the magnitudes of the Bragg peaks in $S(k)$ generally decrease, consistent with increasing disorder of the systems. In addition, $S(k)$ of these nanotubes goes to zero as k goes to zero, but

is not zero at small finite k , indicating that carbon nanotubes with randomly distributed SW defects are hyperuniform, but not stealthy hyperuniform [20]. This is in contrast to defect-free carbon nanotubes, which possess periodic structures that are translationally and rotationally invariant, and thus are known to be stealthy hyperuniform [20]; i.e., their $S(k)$ is not only zero as k goes to zero, but also zero at finite k smaller than the wave number associated with the first Bragg peak in the Fourier space.

V. DENSITY FLUCTUATIONS OF MULTIWALLED NANOTUBES

It can be easily seen that MWNTs consisting of K defect-free zigzag nanotubes with $(n_1, 0)$, $(n_2, 0)$, \dots , $(n_K, 0)$ rolling vectors, respectively, are mapped into two-scale 1D point patterns with $\zeta = \frac{1}{3}$ [19] when projecting onto the cylinder axis of the nanotubes, with $n_1 + n_2 + \dots + n_K$ carbon atoms superimposed onto each other at each point in the 1D point pattern. The number variance of the MWNTs $\sigma_N^2(R)$ can then be determined analytically as

$$\sigma_N^2(R) = (n_1 + n_2 + \dots + n_K)^2\sigma_{N,D}^2(R), \quad (21)$$

where $\sigma_{N,D}^2(R)$ is the number variance of the projected two-scale 1D point patterns with $\zeta = \frac{1}{3}$ [19]. Therefore, $\sigma_N^2(R)$ of defect-free MWNTs consisting of multiple zigzag nanotubes fluctuate around certain constant, and these nanotubes are class-I hyperuniform.

On the other hand, as SW defects are introduced into the nanotubes, the structures gradually transition into amorphous ones, which are reflected in their local number variance $\sigma_N^2(R)$. For example, we show the ensemble-averaged $\sigma_N^2(R)$ for MWNTs consisting of a (3,0) zigzag nanotube and a (5,0) zigzag nanotube at different defect fractions p in Fig. 3(a). At low p , $\sigma_N^2(R)$ exhibits “periodicity” in the window radius R , indicating that the crystalline order is reminiscent in the systems; at large p , the oscillations of $\sigma_N^2(R)$ become much more damped as R increases, suggesting the emergence of

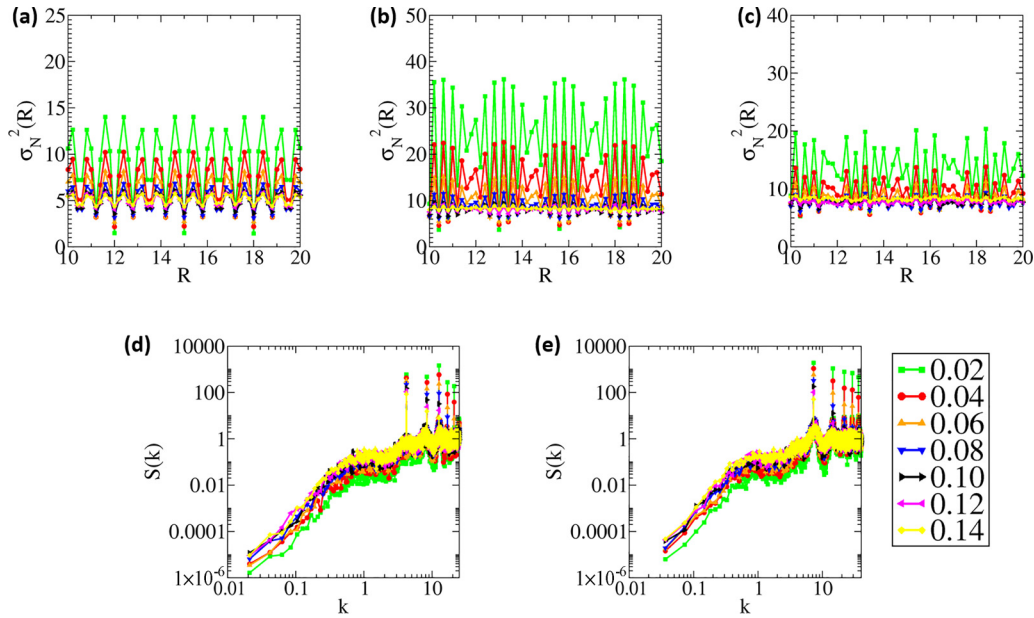


FIG. 3. Local number variances $\sigma_N^2(R)$ (top) and structure factor $S(k)$ (bottom, log-log scale) of defected multiwalled nanotubes at different defect concentrations p . (a) $\sigma_N^2(R)$ of double-walled nanotubes consisting of a (3,0) zigzag nanotube and a (5,0) zigzag nanotube. (b) $\sigma_N^2(R)$ of double-walled nanotubes consisting of a (3,3) armchair nanotube and a (5,5) armchair nanotube. (c) $\sigma_N^2(R)$ of double-walled nanotubes consisting of a (5,0) zigzag nanotube and a (5,5) armchair nanotube. (d) $S(k)$ of double-walled nanotubes consisting of a (3,0) zigzag nanotube and a (5,0) zigzag nanotube. (e) $S(k)$ of double-walled nanotubes consisting of a (3,3) armchair nanotube and a (5,5) armchair nanotube. The results are all averaged over 10 configurations.

truly amorphous states. Interestingly, the variance $\sigma_N^2(R)$ of these MWNTs fluctuates around certain constants as R increases at all investigated p , indicating that these structures are class-I hyperuniform. These behaviors are similar to those in the cases of the SWNTs.

Similarly, MWNTs consisting of K defect-free armchair nanotubes with (n_1, n_1) , (n_2, n_2) , \dots , (n_K, n_K) rolling vectors, respectively, are mapped into single-scale 1D point patterns [19] when projecting onto the cylinder axis of the nanotubes, with $2(n_1 + n_2 + \dots + n_K)$ carbon atoms superimposed onto each other at each point in the 1D point pattern. As a result, the number variance of the MWNTs $\sigma_N^2(R)$ can be theoretically determined as

$$\sigma_N^2(R) = 4(n_1 + n_2 + \dots + n_K)^2 \sigma_{N,S}^2(R), \quad (22)$$

where $\sigma_{N,S}^2(R)$ is the number variance of the projected single-scale 1D pattern. On the other hand, as SW defects are introduced into the nanotubes, the behaviors of these MWNTs consisting of purely armchair nanotubes are similar to those MWNTs consisting of purely zigzag nanotubes. For example, we show the computed $\sigma_N^2(R)$ for MWNTs consisting of a (3,3) armchair nanotube and a (5,5) armchair nanotube at different defect fractions p in Fig. 3(b). Importantly, at all investigated p , the variance $\sigma_N^2(R)$ of these MWNTs fluctuates around certain constants, indicating that these structures are class-I hyperuniform.

Interestingly, MWNTs consisting of both zigzag and armchair nanotubes exhibit different behaviors in their density fluctuations from SWNTs or MWNTs consisting of purely zigzag or armchair nanotubes. For example, as shown in Fig. 3(c), $\sigma_N^2(R)$ of MWNTs consisting of a (5,0) zigzag

nanotube and a (5,5) armchair nanotube exhibit no “periodicity” in the window radius R even at low p , and appear close to those of a limit-periodic set [48]. This is a direct result of the fact that the length of the smallest repeating unit in a defect-free (5,0) zigzag nanotube and that of the smallest repeating unit in a defect-free (5,5) armchair nanotube do not have an integer common multiple, and the 1D projections of the two nanotubes collectively onto the cylinder axis are no longer periodic. Here when placing the observation window in the process of computing $\sigma_N^2(R)$, we restrict the observation window to fall entirely in the range of the (5,5) armchair nanotube in the axial direction, which is smaller than that of the (5,0) zigzag nanotube. We note that while a limit-periodic set is a union of infinite number of single-scale periodic patterns with ever-increasing lattice constants of the form aq^n [48], where a is a constant, q is an integer, and n runs over all possible integers, the projection of a MWNT is a union of a finite number of periodic patterns, which do not need to possess lattice constants in the form of aq^n or be single-scaled.

The results of ensemble-averaged $S(k)$ of MWNTs consisting of a (3,0) zigzag nanotube and a (5,0) zigzag nanotube, and MWNTs consisting of a (3,3) armchair nanotube and a (5,5) armchair nanotube, are shown in Fig. 2(d) and Fig. 2(e), respectively, which all decrease to zero as k goes to zero, regardless of defect concentration p . These results further confirm the hyperuniformity of these nanotubes, and are consistent with the results of $\sigma_N^2(R)$. We note that due to the lack of periodicity of the simulation box in the axial direction of the MWNT consisting of a (5,0) zigzag nanotube and a (5,5) armchair nanotube, $S(k)$ is not well defined for this MWNT, and we do not compute its $S(k)$.

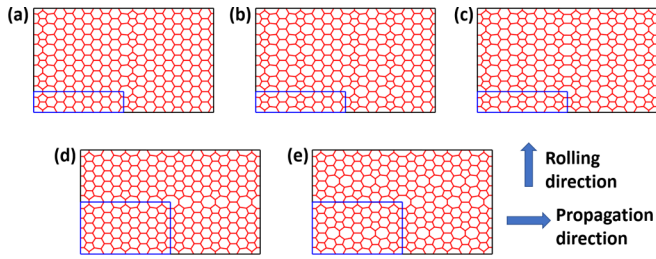


FIG. 4. Two classes of defected graphene sheets with periodic distribution of Stone-Wales defects, which are then rolled into (10,0) nanotubes. Their unit cells are shown by the blue boxes, which are replicated five times in the horizontal direction (propagation direction of the nanotubes) before rolling into the nanotubes, and for clear visualization we only show a portion in the horizontal direction. Top: Defect model I sheets at (a) $p = 0.0167$, (b) $p = 0.0333$, and (c) $p = 0.05$. Bottom: Defect model II sheets at (d) $p = 0.02$ and (e) $p = 0.0333$.

VI. STABILITY AND DENSITY OF STATES OF DISORDERED HYPERUNIFORM CARBON NANOTUBES

We use (10,0) zigzag SWNTs as examples to demonstrate the effect of different concentrations of SW defects on the stability and electronic structure properties of the amorphous SWNTs. Specifically, density functional theory (DFT) [49,50] calculations are performed with the Atomic-orbital Based Ab initio Computation at UStc (ABACUS) package [51,52]. The norm-conserving pseudopotential [53,54] is employed to describe the ion-electron interactions and the valence electron configuration of C is $2s^2 2p^2$. The generalized gradient approximation (GGA) in the form of Perdew-Burke-Ernzerhof (PBE) [55] is used for the exchange-correlation functional. In order to deal with large systems of (10,0) zigzag SWNTs, we employ numerical atomic orbitals (NAOs) in the form of double- ζ plus polarization function (DZP) orbitals as basis sets in our calculations, whose accuracy and consistency have been verified in previous studies [52,56,57]. Specifically, we use $2s2p1d$ NAOs for C, whose radius cutoff is set to 8 bohrs. The energy cutoff is set to 60 Ry. Besides, periodic boundary conditions and a single k point (Γ point) are used. We employ the Gaussian smearing method with the smearing width of 0.001 Ry. Structural optimizations are performed with the conjugated gradient method until forces on each atom are below 0.04 eV/\AA .

We first demonstrate the stability of DHU nanotubes. To this end, we compare the results of the DHU configurations at different defect concentrations p to those of the defect-free counterpart, as well as two other representative models of nanotubes containing periodically distributed SW defects shown in Fig. 4. Specifically, in defect model I we introduce SW defects into a unit cell with 40 carbon atoms shown by the blue box in the top row of Fig. 4, and then replicate the unit cell five times in both horizontal and vertical directions to generate a graphene sheet before rolling up to form (10,0) nanotubes. In defect model II, we introduce SW defects into a unit cell with 100 carbon atoms shown by the blue box in the bottom row of Fig. 4, and then replicate the unit cell five times in the horizontal direction and two times in the vertical directions to generate a graphene sheet before rolling

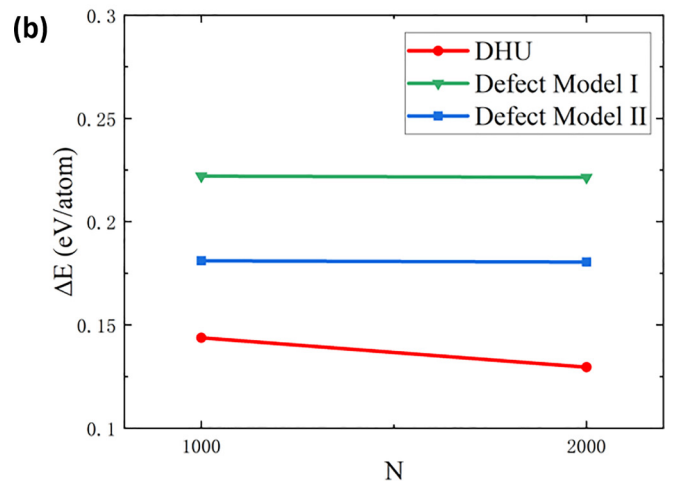
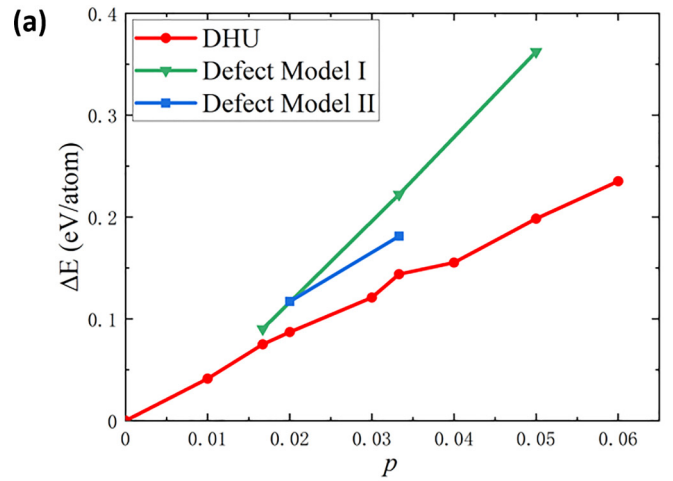


FIG. 5. (a) Excess energy per atom ΔE (difference of the total energy between the amorphous system and the corresponding defect-free state, divided by the number of atoms in the nanotube) of (10, 0) zigzag DHU nanotubes at different SW defect concentrations p , compared to ΔE of two other representative defect nanotube models with periodically distributed SW defects. (b) Excess energy per atom ΔE for (10, 0) zigzag DHU nanotubes and two other representative defect nanotube models with periodically distributed SW defects as a function of system size N at $p = 0.0333$.

up to form (10,0) nanotubes. Due to the constraints associated with the construction of defected nanotube models, we only consider three distinct defect concentrations for defect model I SWNTs, and two concentrations for defect model II SWNTs, which we believe are sufficiently representative.

In particular, we calculate the total energy E (i.e., the sum of interaction energy and electronic kinetic energy of many-body systems) of DHU carbon nanotubes at $T = 0 \text{ K}$ with a wide spectrum of defect concentration p after structural optimizations, as well as the total energy of the two defect models at selected p . Figure 5(a) shows the excess energy per atom ΔE of the aforementioned systems compared to the defect-free carbon nanotube. Since introducing defects always increases the energy of the system, we have $\Delta E > 0$ for all $p > 0$. It can be seen that for all three different defected nanotube models, ΔE increases approximately linearly as

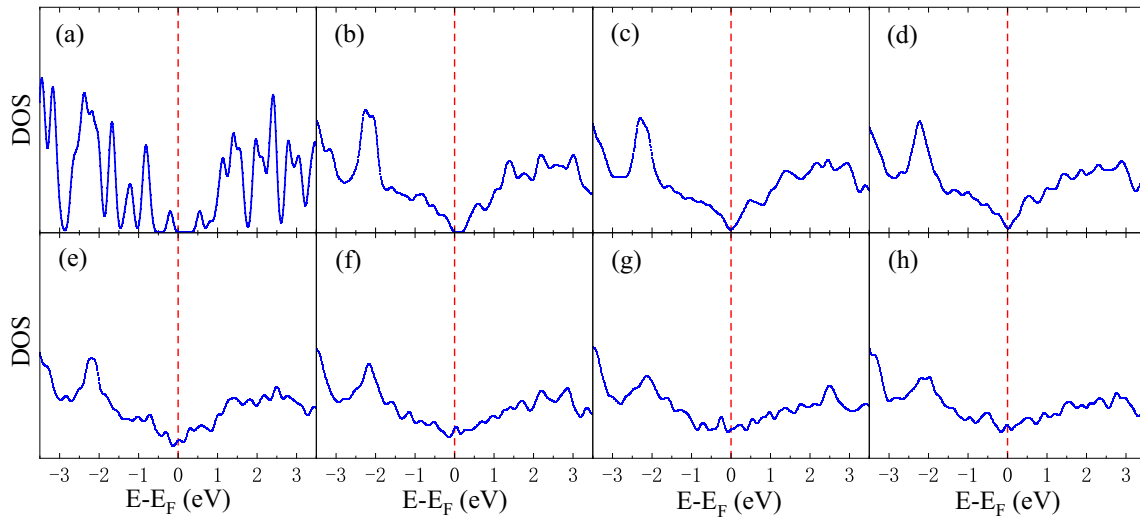


FIG. 6. Density of states (DOS) of (10, 0) zigzag DHU carbon nanotubes computed by PBE functional at defect concentration p : (a) 0.00, (b) 0.01, (c) 0.0167, (d) 0.02, (e) 0.03, (f) 0.04, (g) 0.05, (h) 0.06.

the concentration p increases. The DHU nanotubes appear to possess the lowest ΔE among the three models for the same p values, and possess the smallest slope among the three. This result implies that DHU states are more energetically stable than the two defect models with periodically distributed SW defects. In Fig. 5(b) we also show the excess energy per atom ΔE of the aforementioned systems compared to the defect-free carbon nanotube as a function of the system size N at a given defect concentration $p = 0.0333$. These results suggest that our observation that DHU states are the most energetically stable among the three is robust with respect to finite-size effects.

We further investigate the electronic structures of DHU nanotubes to shed light on the effects of increasing SW defects on the material properties. Figure 6 shows the DOS of (10, 0) zigzag DHU carbon nanotubes computed by the PBE functional at different p as well as the DOS of defect-free carbon nanotubes. It is well known [12,13] that (10,0) nanotubes possess a well-defined band gap at Fermi level, which is captured in our calculations [see Fig. 6(a)]. Increasing disorder in the DHU system (i.e., increasing the amount of SW defects) results in two observed effects on the computed DOS: (i) Closure of the band gap at Fermi level and (ii) broadening and flattening of the DOS, which are consistent with previous computational study of a defected nanotube that is semiconducting in its defect-free state [11]. This trend is also similar to the observations in DHU 2D materials [14,15]. Specifically, the band gap is closed at $p = 0.0167$, suggesting the presence of the semiconductor-to-metal transition around this defect concentration. Moreover, as p increases the DOS becomes more and more extended, converging to a metallic characteristic, as shown by the electron densities at the Fermi level in Fig. 7. We note that although the exact values of the band gaps could be underestimated by PBE functional compared with the actual values, the qualitative behavior of the DOS in DHU nanotubes suggests a semiconductor-to-metal transition should be robust.

It is also noteworthy that as mentioned above, in this work we *randomly* introduce SW defects into the originally perfect

crystalline systems; i.e., there is essentially no correlation between the locations of the defect centers, in particular at low and intermediate defect concentrations [15]. This setting mimics typical experimental realizations of the SW defects, which are introduced by random proton radiations [6]. Moreover, we consider the periodic defect models in order to obtain insights on the effects of SW defect distribution. Intuitively, in these periodic models, the defects are more “clustered” compared to the random distribution model, and the remaining region is free of defects (i.e., crystalline). We speculate that the clustered defects lead to larger local distortion of the covalent bonds in the defected region and, thus, increased energy of the system. The two representative periodic models that we have numerically investigated confirm our speculation. However, we note that this does not imply that the random

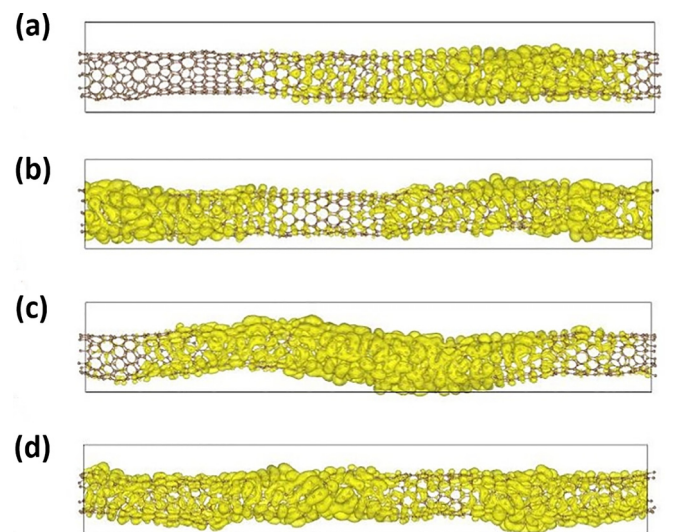


FIG. 7. Electron densities at the Fermi level of (10, 0) zigzag nanotubes at different p . The yellow surface represents isosurface of 1.0×10^{-10} atomic unit. (a) $p = 0.03$. (b) $p = 0.04$. (c) $p = 0.05$. (d) $p = 0.06$.

defect distribution model would possess the lowest energy over all defect distributions. With the development of new experimental techniques, other correlated defect distributions could be realized, which may possess lower energy than the random defect distribution model in the current work.

VII. CONCLUSIONS AND DISCUSSION

In this work, we generalized the concept of hyperuniformity to structurally characterize quasi-one-dimensional materials, which in the context of hyperuniformity can be viewed as one-dimensional projections of higher-dimensional structures along the axial direction. As a proof of concept, we systematically investigated the density fluctuations across length scales in amorphous carbon nanotubes containing different amounts of Stone-Wales topological defects, which can be constructed by rolling up defected graphene sheets. We demonstrated that all amorphous nanotubes containing SW defects studied here are hyperuniform; i.e., the normalized infinite-wavelength density fluctuations are completely suppressed, regardless of the diameter, rolling axis, number of rolling sheets, and defect fraction of the nanotubes. Disordered hyperuniformity is a recently discovered exotic state of matter. Using DFT simulations, we also showed that these amorphous carbon nanotubes with randomly distributed Stone-Wales defects are energetically more stable than their ordered counterparts with periodically distributed Stone-Wales defects. We also demonstrated that the electronic band gap closes for a semiconducting zigzag nanotube as Stone-Wales defects are randomly introduced into the carbon nanotubes by determining the density of states near the Fermi level. Our structural study of amorphous nanotubes strengthens our fundamental understanding of these quasi-1D materials, and suggests possible exotic physical properties, as endowed by the unique disordered hyperuniformity feature.

Our findings on the effect of the projection operation on the hyperuniformity property of the graphene sheets may also shed light on our understanding of the general effect of dimensionality reduction on the preservation of (non)hyperuniformity, as projection is a common type of dimensionality reduction operation. While we conjecture that projection should preserve (non)hyperuniformity of isotropic higher-dimensional structures since each dimension contributes equally to the density fluctuations in the isotropic cases, this is definitely not always the case for anisotropic structures. This can be seen from the following example of anisotropic point patterns, where the points are placed randomly in the vertical direction, but are constrained to discrete equally distributed lattice sites in the horizontal direction with each site having the same number of points, as shown in Fig. 8. The projection of this two-dimensional point pattern along the vertical direction is a one-dimensional Poisson point pattern, which is known to be nonhyperuniform [19]. On the other

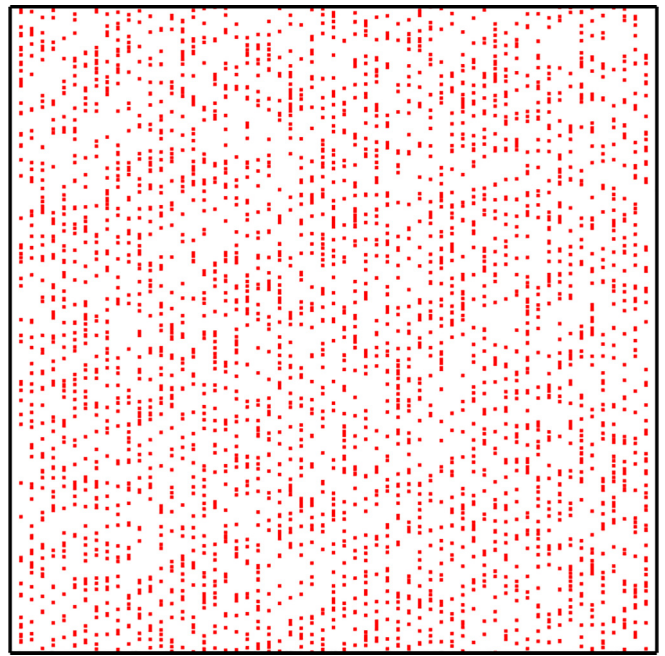


FIG. 8. An anisotropic point pattern where the points are placed randomly in the vertical direction, but are constrained to discrete equally distributed lattice sites in the horizontal direction with each site having the same number of points. The projection of this point pattern is hyperuniform when projected along the horizontal direction, and nonhyperuniform when projected along the vertical direction.

hand, the projection of this two-dimensional point pattern along the horizontal direction is a single-scale lattice in one dimension, which is known to be class-I hyperuniform [19]. This example shows that the projection of an anisotropic point could be hyperuniform when projected in one direction, but nonhyperuniform when projected along another direction. It is also noteworthy that many quasicrystals can be constructed by a projection from higher dimensions [20], e.g., the Fibonacci chain, which preserves the hyperuniformity of the structures in the higher dimensions before projection, similar to the case of carbon nanotubes.

ACKNOWLEDGMENTS

Y.L. and M.C. were supported by the National Science Foundation of China under Grants No. 12122401 and No. 12074007. Parts of the numerical simulations were performed on the High Performance Computing Platform of CAPT. H.Z. is grateful for the start-up funds from ASU. This research also used computational resources of the Agave Research Computer Cluster of ASU and the Texas Advanced Computing Center under Contract No. TG-DMR170070.

- [1] S. Iijima, *Nature (London)* **354**, 56 (1991).
- [2] S. Iijima and T. Ichihashi, *Nature (London)* **363**, 603 (1993).
- [3] S. J. Tans, A. R. M. Verschueren, and C. Dekker, *Nature (London)* **393**, 49 (1998).

- [4] P. G. Collins, A. Zettl, H. Bando, A. Thess, and R. E. Smalley, *Science* **278**, 100 (1997).
- [5] J. Kong, N. R. Franklin, C. Zhou, M. G. Chapline, S. Peng, K. Cho, and H. Dai, *Science* **287**, 622 (2000).

- [6] L. G. Zhou and S.-Q. Shi, *Appl. Phys. Lett.* **83**, 1222 (2003).
- [7] J. A. Robinson, E. S. Snow, Ş. C. Bădescu, T. L. Reinecke, and F. K. Perkins, *Nano Lett.* **6**, 1747 (2006).
- [8] B. J. Gifford, S. Kilina, H. Htoon, S. K. Doorn, and S. Tretiak, *Acc. Chem. Res.* **53**, 1791 (2020).
- [9] S. B. Sinnott and R. Andrews, *Crit. Rev. Solid State Mater. Sci.* **26**, 145 (2001).
- [10] A. J. Stone and D. J. Wales, *Chem. Phys. Lett.* **128**, 501 (1986).
- [11] V. H. Crespi, M. L. Cohen, and A. Rubio, *Phys. Rev. Lett.* **79**, 2093 (1997).
- [12] S. Azadi, R. Moradian, and A. M. Shafae, *Comput. Mater. Sci.* **49**, 699 (2010).
- [13] P. Partovi-Azar, S. P. Jand, A. Namiranian, and H. Rafii-Tabar, *Comput. Mater. Sci.* **79**, 82 (2013).
- [14] Y. Zheng, L. Liu, H. Nan, Z.-X. Shen, G. Zhang, D. Chen, L. He, W. Xu, M. Chen, Y. Jiao *et al.*, *Sci. Adv.* **6**, eaba0826 (2020).
- [15] D. Chen, Y. Zheng, L. Liu, G. Zhang, M. Chen, Y. Jiao, and H. Zhuang, *Proc. Natl. Acad. Sci. USA* **118**, e2016862118 (2021).
- [16] D. Chen, Y. Zheng, C.-H. Lee, S. Kang, W. Zhu, H. Zhuang, P. Y. Huang, and Y. Jiao, *Phys. Rev. B* **103**, 224102 (2021).
- [17] Y. Zheng, D. Chen, L. Liu, Y. Liu, M. Chen, H. Zhuang, and Y. Jiao, *Phys. Rev. B* **103**, 245413 (2021).
- [18] D. Chen, Y. Zheng, and Y. Jiao, *Phys. Rev. B* **104**, 174101 (2021).
- [19] S. Torquato and F. H. Stillinger, *Phys. Rev. E* **68**, 041113 (2003).
- [20] S. Torquato, *Phys. Rep.* **745**, 1 (2018).
- [21] C. E. Zachary and S. Torquato, *J. Stat. Mech.: Theory Exp.* (2009) P12015.
- [22] A. Gabrielli, M. Joyce, and F. S. Labini, *Phys. Rev. D* **65**, 083523 (2002).
- [23] C. E. Zachary, Y. Jiao, and S. Torquato, *Phys. Rev. Lett.* **106**, 178001 (2011).
- [24] Y. Jiao, T. Lau, H. Hatzikirou, M. Meyer-Hermann, J. C. Corbo, and S. Torquato, *Phys. Rev. E* **89**, 022721 (2014).
- [25] D. Chen, Y. Jiao, and S. Torquato, *J. Phys. Chem. B* **118**, 7981 (2014).
- [26] C. E. Zachary and S. Torquato, *Phys. Rev. E* **83**, 051133 (2011).
- [27] S. Torquato, G. Zhang, and F. H. Stillinger, *Phys. Rev. X* **5**, 021020 (2015).
- [28] R. Kurita and E. R. Weeks, *Phys. Rev. E* **84**, 030401(R) (2011).
- [29] R. Dreyfus, Y. Xu, T. Still, L. A. Hough, A. G. Yodh, and S. Torquato, *Phys. Rev. E* **91**, 012302 (2015).
- [30] R. L. Jack, I. R. Thompson, and P. Sollich, *Phys. Rev. Lett.* **114**, 060601 (2015).
- [31] J. H. Weijs, R. Jeanneret, R. Dreyfus, and D. Bartolo, *Phys. Rev. Lett.* **115**, 108301 (2015).
- [32] Y. Jiao, *Physica A* **585**, 126435 (2022).
- [33] S. Torquato, A. Scardicchio, and C. E. Zachary, *J. Stat. Mech.: Theory Exp.* (2008) P11019.
- [34] R. P. Feynman and M. Cohen, *Phys. Rev.* **102**, 1189 (1956).
- [35] A. Mayer, V. Balasubramanian, T. Mora, and A. M. Walczak, *Proc. Natl. Acad. Sci. USA* **112**, 5950 (2015).
- [36] M. Hejna, P. J. Steinhardt, and S. Torquato, *Phys. Rev. B* **87**, 245204 (2013).
- [37] R. Xie, G. G. Long, S. J. Weigand, S. C. Moss, T. Carvalho, S. Roorda, M. Hejna, S. Torquato, and P. J. Steinhardt, *Proc. Natl. Acad. Sci. USA* **110**, 13250 (2013).
- [38] M. A. Klatt, J. Lovrić, D. Chen, S. C. Kapfer, F. M. Schaller, P. W. A. Schönhofer, B. S. Gardiner, A. Smith, G. E. Schröder-Turk, and S. Torquato, *Nat. Commun.* **10**, 811 (2019).
- [39] D. Hexner and D. Levine, *Phys. Rev. Lett.* **118**, 020601 (2017).
- [40] D. Hexner, P. M. Chaikin, and D. Levine, *Proc. Natl. Acad. Sci. USA* **114**, 4294 (2017).
- [41] J. H. Weijs and D. Bartolo, *Phys. Rev. Lett.* **119**, 048002 (2017).
- [42] Q.-L. Lei, M. P. Ciamarra, and R. Ni, *Sci. Adv.* **5**, eaau7423 (2019).
- [43] Q.-L. Lei and R. Ni, *Proc. Natl. Acad. Sci. USA* **116**, 22983 (2019).
- [44] Y. A. Gerasimenko, I. Vaskivskiy, M. Litskevich, J. Ravnik, J. Vodeb, M. Diego, V. Kabanov, and D. Mihailovic, *Nat. Mater.* **18**, 1078 (2019).
- [45] S. Sakai, R. Arita, and T. Ohtsuki, *Phys. Rev. Res.* **4**, 033241 (2022).
- [46] G. Rumi, J. Aragón Sánchez, F. Elías, R. Cortés Maldonado, J. Puig, N. R. Cejas Bolecek, G. Nieva, M. Konczykowski, Y. Fasano, and A. B. Kolton, *Phys. Rev. Res.* **1**, 033057 (2019).
- [47] J. Aragón Sánchez, R. Cortés Maldonado, N. R. Cejas Bolecek, G. Rumi, P. Pedrazzini, M. I. Dolz, G. Nieva, C. J. van der Beek, M. Konczykowski, C. D. Dewhurst *et al.*, *Commun. Phys.* **2**, 143 (2019).
- [48] E. Oğuz, J. E. S. Socolar, P. J. Steinhardt, and S. Torquato, *Acta Cryst.* **A75**, 3 (2019).
- [49] P. Hohenberg and W. Kohn, *Phys. Rev.* **136**, B864 (1964).
- [50] W. Kohn and L. J. Sham, *Phys. Rev.* **140**, A1133 (1965).
- [51] M. Chen, G. C. Guo, and L. He, *J. Phys.: Condens. Matter* **22**, 445501 (2010).
- [52] P. Li, X. Liu, M. Chen, P. Lin, X. Ren, L. Lin, C. Yang, and L. He, *Comput. Mater. Sci.* **112**, 503 (2016).
- [53] D. R. Hamann, *Phys. Rev. B* **88**, 085117 (2013).
- [54] M. Schlipf and F. Gygi, *Comput. Phys. Commun.* **196**, 36 (2015).
- [55] J. P. Perdew, K. Burke, and M. Ernzerhof, *Phys. Rev. Lett.* **77**, 3865 (1996).
- [56] Y. Liu, X. Liu, and M. Chen, *J. Nucl. Mater.* **545**, 152733 (2021).
- [57] Y. Liu, X. Ding, M. Chen, and S. Xu, *Phys. Chem. Chem. Phys.* **24**, 15511 (2022).